Accepted Manuscript

Title: Rapid synthesis of BiOBr$_x$I$_{1−x}$ photocatalysts: Insights to the visible-light photocatalytic activity and strong deviation from Vegard's Law

Authors: Liang Kong, Junqiu Guo, Joshua W. Makepeace, Tiancun Xiao, Heather F. Greer, Wuzong Zhou, Zheng Jiang, Peter P. Edwards

Please cite this article as: Kong L, Guo J, Makepeace JW, Xiao T, Greer HF, Zhou W, Jiang Z, Edwards PP, Rapid synthesis of BiOBr$_x$I$_{1-x}$ photocatalysts: Insights to the visible-light photocatalytic activity and strong deviation from Vegard's Law, *Catalysis Today* (2019), https://doi.org/10.1016/j.cattod.2019.02.013

Rapid synthesis of BiOBr$_x$I$_{1-x}$ photocatalysts: Insights to the visible-light photocatalytic activity and strong deviation from Vegard's Law

Liang Kong,[a,b] Junqiu Guo,[c] Joshua W. Makepeace,[a] Tiancun Xiao,[a] Heather F. Greer,[d] Wuzong Zhou,[d]

Zheng Jiang,[c]* and Peter P. Edwards[a]*

[a.] Inorganic Chemistry Laboratory, University of Oxford, Oxford, OX1 3QR, UK

[b.] Center for Applied Energy Research, University of Kentucky, Lexington, KY, 45011, US

[c.] School of Engineering, Faculty of Engineering and Physical Sciences, University of Southampton, Highfield, Southampton, SO17 1BJ, UK

[d.] School of Chemistry, University of St Andrews, North Haugh, St Andrews, KY16 9ST, UK

Corresponding Authors: **z.jiang@soton.ac.uk** (ZJ), **peter.edwards@chem.ox.ac.uk**(PPE)

Graphic Abstract
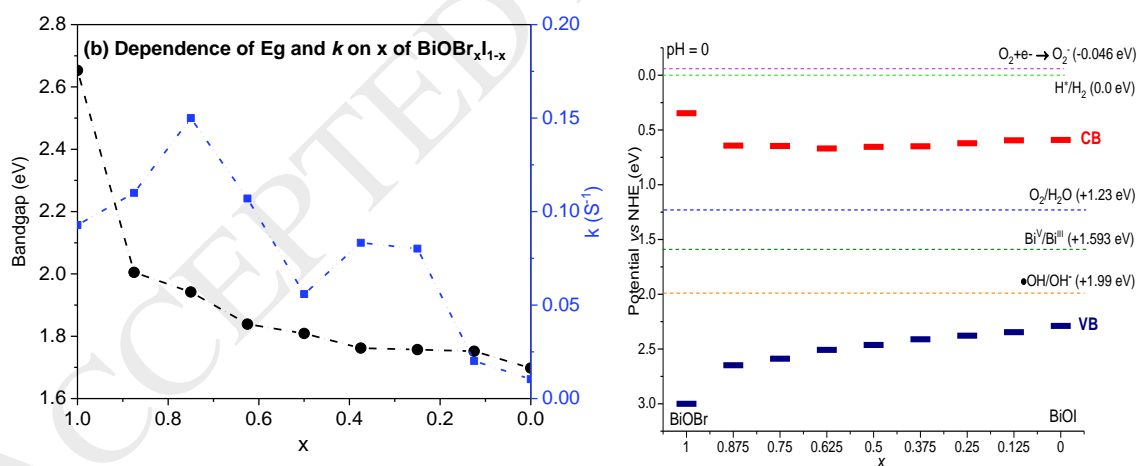
A rapid ultrasonication synthesis was demonstrated to synthesise BiOBr$_x$I$_{1-x}$ solid solution visible-light-responsive photocatalysts, which displayed strong deviations of crystal and band structures from Vegard's law.

Research Highlights

- A rapid ultrasonication synthesis was adopted to prepare $BiOBr_xI_{1-x}$ solid solutions;

- Lattice parameters of the $BiOBr_xI_{1-x}$ solid solutions strongly deviate from Vegard's law;

- The nonlinear dependence of bandgaps on Br/I ratio are clarified;

- Tuning I/Br ratios can tune both the VBM and CBM of the $BiOBr_xI_{1-x}$ solid solutions;

- The Bi-rich $BiOBr_xI_{1-x}$ solid solutions are superior to BiOBr in photodegradation of RhB

Abstract

A series of visible-light-responsive $BiOBr_xI_{1-x}$ solid solutions were prepared by a rapid and efficient ultrasonication synthesis and applied in photodegradation of Rhodamine B in aqueous solution. The detailed characterisations showed that the lattice parameters and their band structures of the $BiOBr_xI_{1-x}$ solid solutions significantly deviated from the well-established Vegard's law for solid solution materials. The Mulliken electronegativity and valence band XPS analyses revealed that the substitution of Br by less electronegative iodine can simultaneously modulate the edges of conductance and valence band of the BiOBr, leading to nonlinear dependence of bandgap (Eg) on the halogen anion concentrations. Although the solid solution displayed superior RhB photodegration activity to BiOI, only Br-rich $BiOBr_xI_{1-x}$ solid solutions (x>0.5) were more active than BiOBr and BiOI, with the optimal one is $BiOBr_{0.75}I_{0.25}$. The Br-dependence of bandstructure and photocatalytic activity for the $BiOBr_xI_{1-x}$ solid solutions as well as their rate-limiting radical species were also clarified based on experimental and theoretical analyses.

KEYWORDS $BiOBr_xI_{1-x}$, solid solution, band edges, visible light photocatalysis

1. Introduction

2

As one of the promising technologies with great potentials for energy and environment sustainability, solar-driven photocatalysis stringently requires effective semiconductor photocatalysts of broad absorption to visible-light, significant reactivity and remarkable stability under sunlight illumination [1-6]. Although exploring novel photocatalysts with stable crystal structures is appealing and exciting, tuning the electronic band structure of existing stable photocatalysts without significant change of crystallographic polymorph is a rather reliable and simple approach to tailoring their function. This is because the band gap (E_g) determines light absorption and the most effective photocatalytic active species on the photocatalyst originate from the photogenerated charge carriers on the band edges: electrons at the conduction band minimum (VBM) and/or photogenerated holes at valence band maximum (CBM)[7].

So far, the most stable and widely applied photocatalyst is still TiO_2, which can only be activated by UV light. In order to promote the visible-light absorption of TiO_2, a variety of methodologies have been attempted extensively and successfully, including impurity doping and surface decoration to form either multiple-semiconductor junctions (heterojunctions or homojunctions) or metal/semiconductor Mott-Schottky junctions.[8-10] However, the precise modulation of electronic structure of TiO_2 and its derived photocatalysts (eg. perovskite titanate [11, 12]) encounters outstanding problems, such as tedious and costly preparation processes, detrimental stability or significant recombination of photogenerated charge carriers. [13]

As a class of V-VI-VII compound semiconductors, the bismuth oxyhalides (BiOX, X=Cl, Br, I) have recently emerged as efficient and stable photocatalysts for the photodegradation of various organic dyes [14, 15] and the generation of solar fuels [7]. Moreover, the unique lamellar structures of BiOXs enable fine tuning their band structures by host of multiple halide anions to form solid solution photocatalysts [16, 17]. However, the variations of crystallography

3

and bandstructure due to the coexistence of multiple halides, in particular the dependence of band edges on the halide anions, necessitate in-depth investigation.

Here we report the band structure-controlled $BiOBr_xI_{1-x}$ solid solutions prepared *via* a rapid ultrasonication synthesis method in aqueous media. The as-synthesised $BiOBr_xI_{1-x}$ samples exhibit composition-dependent optical properties and activity in visible-light photodegradation of RhB, which are correlated with their band structures.

2. Experimental

2.1 Synthesis of $BiOBr_xI_{1-x}$ solid solutions

$Bi(NO_3)_3 \cdot 5H_2O$ was first dissolved in 50 mL aqueous solution containing 5 mL acetic acid under magnetic stirring. The $Bi(NO_3)_3$ aqueous solution was poured into 50 mL of KX solution containing stoichiometric amount of KX (KBr and/or KI) and remained under ultrasonication (2 kHz) for 0.5 h. The color of the precipitate changes from off-white to orange in line with the Br/I molar ratios. The collected precipitates were washed with distilled water and ethanol before drying overnight in an oven maintaining at 80 °C.

2.2 Characterisations of $BiOBr_xI_{1-x}$

Powder X-ray diffraction (XRD) measurements of all the prepared samples were performed on a PANalytical X'Pert PRO diffractometer in Bragg-Brentano geometry using monochromatised Cu Kα1 (λ=0.15418 nm) radiation under 45 kV, 40 mA, and scanning over 5° to 60° two-theta range. Pawley analysis of the resulting diffraction data was performed using the TOPAS Academic software package[18]. UV-vis diffuse reflectance spectra were recorded on a Varian Cary 5000 UV-visible-NIR spectrometer with a scan rate of 600 nm·min^{-1}. Scanning electron microscopy was performed on a Jeol JSM 5600 SEM with an accelerating voltage of 4.0 kV at the University of St Andrews, UK.

4

X-ray photoemission spectroscopy (XPS) measurements were recorded on a Scienta ESCA300 XPS spectrometer at the National Centre for Electron Spectroscopy and Surface Analysis (NCESS), Daresbury Laboratory, UK. X-rays of energy hv=1486.6 eV was using a monochromatic rotating anode Al-Kα source and a charge neutraliser. The ejected photoelectrons were analysed by a 300 mm mean-radius spherical-sector electron energy analyser with 0.8 mm slits at a pass energy of 150 eV. The effective instrumental resolution is 0.45 eV, as derived from the Gaussian deconvolution of the analyser broadening and the natural line width of the X-ray source (0.27 eV). All the binding energies were referenced to the C 1s peak at 284.5 eV of the adventitious surface carbon. Core level of Bi 4f, Br 3d, I 3d, C 1s and Valence Band Maximum (VBM) were identified individually. The VB edge potential of a semiconductor at the point of zero charge can be expressed empirically *via* Mulliken electronegativity theory.[19]

2.3 Photocatalytic reaction

The photocatalytic activities of the BiOBr$_x$I$_{1-x}$ materials were evaluated by decomposing RhB under visible light irradiation. The optical system used for the photocatalytic reaction consisted of an overhead 300 W Xenon lamp (PLS-SXE 300, Beijing TrustTech) equipped with a UV cutoff filter (UVCUT 400, Beijing TrustTech), which was attached to the lamp source to remove all incoming wavelengths shorter than 400 nm to ensure irradiation with visible light only. In each experiment, reaction suspensions were prepared by adding 0.1 g of photocatalysts to 100 mL of RhB in aqueous solution (20 mg/L). Prior to irradiation, the suspensions were stirred in the dark for 1 hour to ensure the establishment of adsorption–desorption equilibrium of the dye on the catalysts' surfaces. During the irradiation process, approximately 3 mL of suspension was collected at 10 minute intervals and then centrifuged (14000 rpm, 4 minutes) to remove the photocatalyst particles. The collected supernatant solutions were analysed by a Perkin-Elmer Lambda 750S UV-visible spectrophotometer. The characteristic absorbance of RhB at 553 nm was used to determine the concentration of RhB because the absorbance is a linear function of

5

RhB concentration. Hence, the photocatalytic activity of the $BiOBr_xI_{1-x}$ photocataysts can be assessed by comparing the adsorption–desorption equilibrium concentrations (C_0) of RhB before irradiation and the temporal concentration (C).

3. Results and Discussions

3.1 Crystalline phase
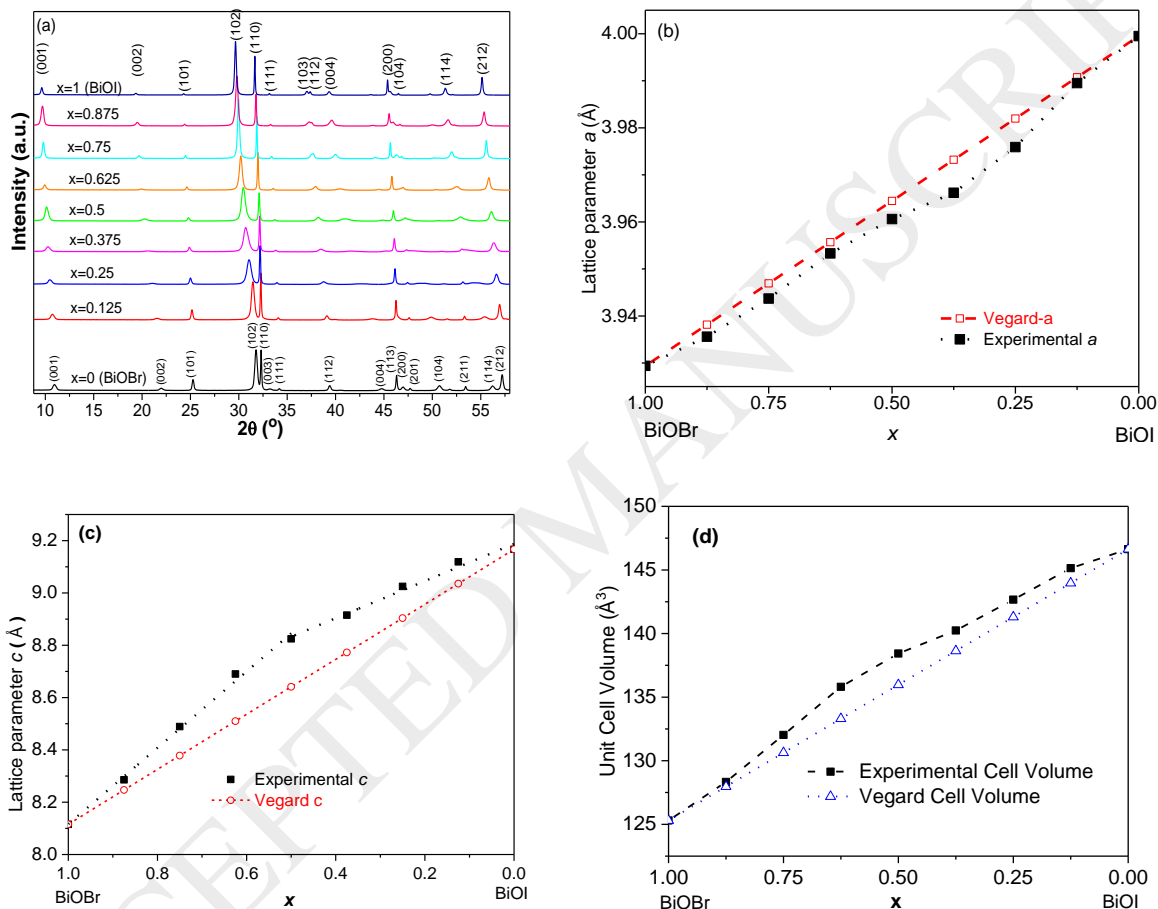
Figure 1. XRD patterns of $BiOBr_xI_{1-x}$ materials (a) and the plots of experimental and fitted (by Vegard law) lattice parameters of (b) *a,* (c) *c* and (d) unit cell volume versus Br concentration

The XRD patterns of as-synthesised BiOBr and BiOI (for x=1.0 and x=0.0) (Figure 1a) well agree with the BiOBr (JCPDS 73-2061) and BiOI (JCPDS 01-0445) crystals in tetragonal phase and *P4/nmm space group* [9, 20]. The characteristic peaks gradually shift to smaller angles as

6

increasing iodine concentration, which is due to the larger ionic radius of iodine (2.20 Å) than

bromide (1.96 Å). The gradual shifts of the XRD peaks and the symmetric peak shapes suggest

that the as-synthesised $BiOBr_xI_{1-x}$ samples are solid solutions rather than the mixtures of BiOBr

and BiOI [16, 20, 21]. The increase of iodine concentration in the $BiOBr_xI_{1-x}$ solid solutions also

leads to gradual increases of crystalline lattice parameters (*a*, *c* and unit cell volume) (Table 1).

Such expansions in lattice parameters further confirm that the iodine was successfully

incorporated into BiOBr lattice.[22] In binary metal solid solutions, the unlimited mutual solubility

can be formed when the difference in their ionic radii is within 15%, whist such rule can be

extended to the general case of solid solutions with larger or smaller radius deviation for specific

system[23]. For the $BiOBr_xI_{1-x}$ materials, the difference between the Br and I ionic radii (Br=1.95,

I=2.20Å) is approximately 12%, hence they can form stable solid solutions.

Table 1. Lattice parameters, electronegativity χ, band gap energy E_g (in eV), energy positions of

band edges (E_{VBM} and E_{CBM}, in eV), and reaction kinetics of the $BiOBr_xI_{1-x}$ materials

x	a (Å)	c (Å)	a/c	V (Å³)	χ (eV)	E_g [a]	E_{VBM}	E_{CBM}	k_{RhB} (min⁻¹·g⁻¹)[b]
1.000	3.9294(2)	8.1154(5)	0.484	125.3033	6.1739	2.653	3.00	0.347	0.0928
0.875	3.9356(3)	8.2854(9)	0.475	128.3321	6.1441	2.005	2.648	0.643	0.1100
0.750	3.9437(6)	8.489(2)	0.465	132.0275	6.1145	1.942	2.588	0.646	0.1500
0.625	3.9533(7)	8.690(7)	0.455	135.8124	6.0850	1.839	2.508	0.669	0.1070
0.500	3.9606(5)	8.8248(2)	0.449	138.4289	6.0556	1.809	2.463	0.654	0.0559
0.375	3.9662(4)	8.915(1)	0.445	140.2396	6.0264	1.762	2.411	0.649	0.0833
0.250	3.9759(3)	9.0250(9)	0.441	142.6652	5.9973	1.757	2.378	0.621	0.0802
0.125	3.9895(5)	9.119(1)	0.438	145.139	5.9684	1.752	2.346	0.594	0.0201
0.000	3.9995(1)	9.1669(4)	0.436	146.6337	5.9396	1.698	2.289	0.591	0.0104

[a] E_g was derived from $E_g=1239.8/\lambda_g$, where λ_g is the absorption edge in the UV-vis spectrum. The E_{VBM}

and E_{CBM} are estimated using Mulliken electronegativity method[16].

As for perfect solid solution (A1-xBx) the lattice parameters follow Vegard's rule in theory[24], as expressed as eq. 1:

$$t(x) = t_A (1 - x) + x t_B = t_A + x(t_B - t_A) \qquad \ldots\ldots\ldots\ldots(1)$$

where t_A and t_B are respective to the lattice parameters of end members A and B. [24] In the present work, A and B are BiOBr and BiOI, respectively. As plotted in Fig.1 b and c, the increase of I^- concentration in the $BiOBr_xI_{1-x}$ causes almost linear increase in the experimental *a* lattice parameter (slightly negative deviation with slope of ~0.07), while the increase in the *c* parameter is much larger than the Vegard-*c* values (in two larger slopes). The more significant lattice deviation from Vegard's law along crystal z crystal axis is reasonable, [24] because the inter-layered halide anions interact with the $[Bi_2O_2]^{2+}$ slabs in weak Van de Waal's force. The Van de Waal's force is sensitive to X^- radius and exerts less influential to the covalent Bi-O bonding that determines a lattice parameter. It is notable that the expansion of the *c* parameter appears to follow two linear trends: the *c* parameters increase faster as decreasing x, then slow down as further increasing iodine concentration, and the maximum deviation observed at x=0.5. As a consequence, the unit cell volumes ($V = a^2c$) of the $BiOBr_xI_{1-x}$ solid solution photocatalysts also deviate from theoretical values (Fig.1 d), indicating the crystal structure of the solid solutions distorted from tetragonal phases, with greatest deviation at x=0.5. The (*hk*0) reflections in the diffraction data are very sharp, while *l*≠0 reflections show significant broadening in the intermediate x values, indicating a degree of compositional variation in the materials.

3.2 Optical property

8
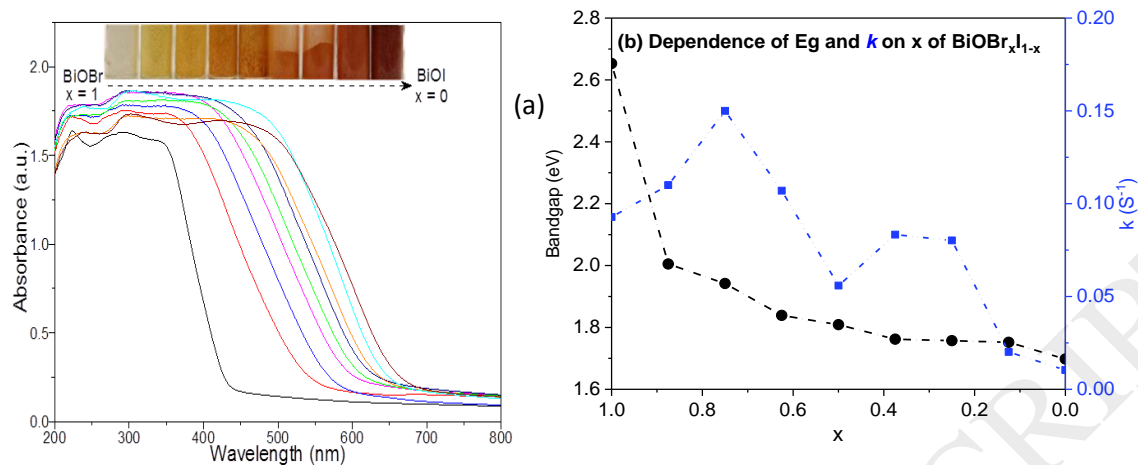
Figure 2. The Br/I ratio dependence of UV-Vis absorption spectra (a) and bandgaps (b) of the $BiOBr_xI_{1-x}$ solid solutions

When increasing structural I^- concentration of the $BiOBr_xI_{1-x}$ samples, as shown in the diffuse reflectance spectra in Fig. 2a, their absorption edges significantly redshift from 440 nm for BiOBr to 670 nm of BiOI, which is consistent with their gradual colour evolution (photos inserted in Fig.2a). The sharp adsorption edges of the $BiOBr_xI_{1-x}$ samples reveal they are due to band gap transition rather than midgap absorption because the midgap transitions ought to be tailed spectra.[25] The bandgaps of pure BiOBr and BiOI samples are well consistent with the Eg reported previously.[16, 20] Moreover, as increasing iodine concentration (x decreasing), the band gap energies (E_g) of the $BiOBr_xI_{1-x}$ solid solutions nonlinearly decrease from 2.81 eV of BiOBr and 1.85 eV of BiOI (Fig.2b), which indicates the dependence of bandgap on halide concentration is nonlinear and highly dependent on the iodine concentration. The detailed analysis of band structure dependence on iodine concentration is discussed in section 3.5.

3.3 Morphology

9
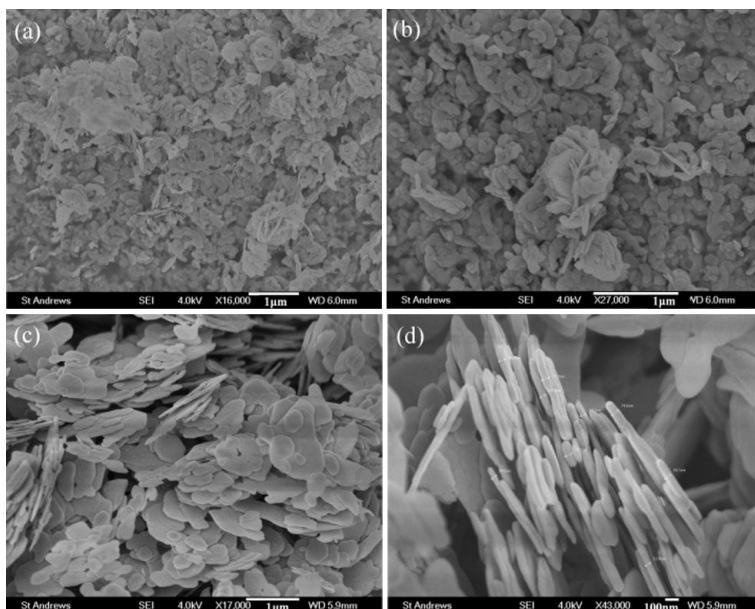
Figure 3. SEM images of (a) BiOBr, (b) $BiOBr_{0.5}I_{0.5}$, (c) $BiOBr_{0.875}I_{0.125}$, and (d) BiOI

The morphologies of the as-synthesised $BiOBr_xI_{1-x}$ solid solutions are shown in Fig. 3a~d, where once can see that all the samples consist of flake-like particles, with particle size gradually increasing from 200 to 500 nm as iodine concentration increasing. There is no obvious difference between the BiOBr and BiOI thin flakes, and their thickness is approximately 100 nm. Therefore, the composition-dependent photocatalytic performance (see section 3.6) of the solid solution samples should not be originated from the morphology of the $BiOBr_xI_{1-x}$ samples.

3.4 Surface Elemental Composition

10
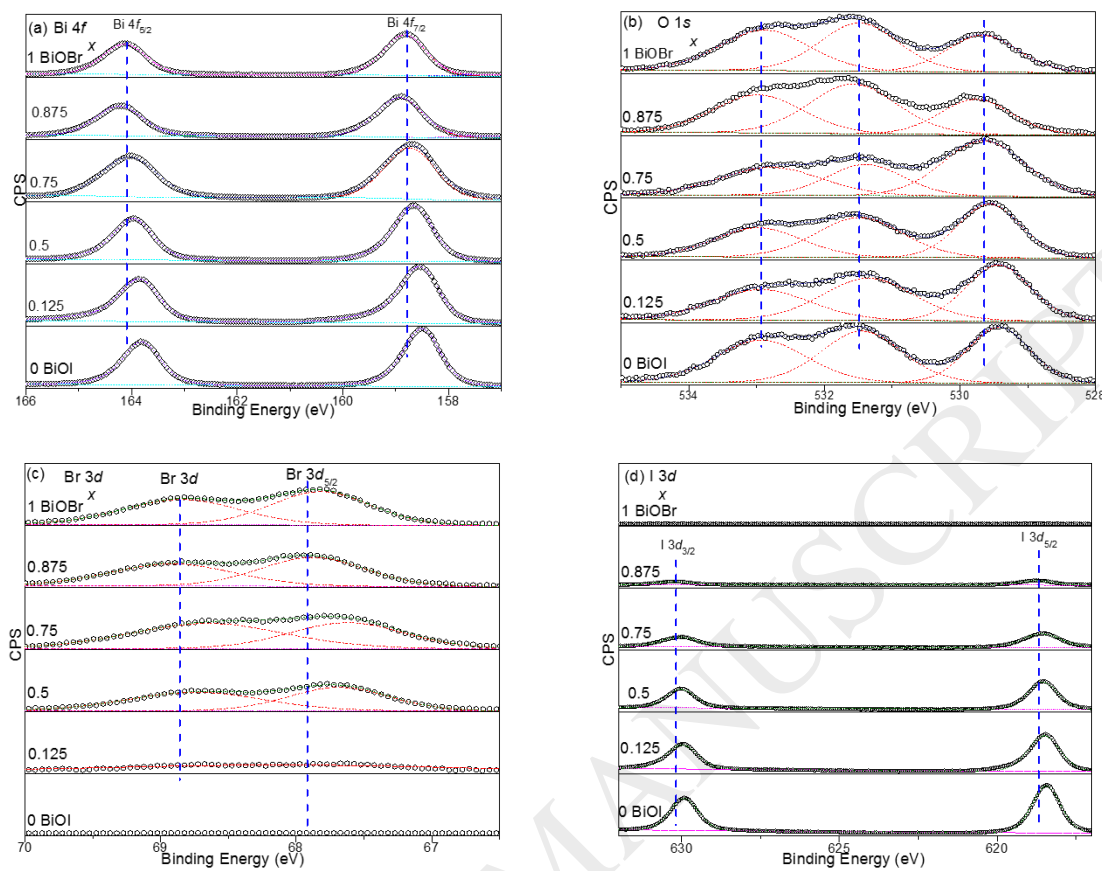
Figure 4. XPS spectra of (a) Bi 4*f*, (b) O 1*s*, (c) Br 3*d*, (d) I 3*d* of the BiOBr$_x$I$_{1-x}$ samples where x=1, 0.875, 0.75, 0.5, 0.125, and 0

The surface elemental composition and element valence states for the BiOBr$_x$I$_{1-x}$ samples were identified by high-resolution X-ray photoelectron spectroscopy (XPS) (Fig. 4a–d). In the Bi 4*f* XPS spectra (Fig. 4a), the two strong peaks located at binding energies (B.E.) of 164.1 and 158.7 eV are due to characteristic Bi 4$f_{5/2}$ and 4$f_{7/2}$ core level emissions of Bi^{3+} cations in the BiOBr$_x$I$_{1-x}$ solid solutions.[26] With increasing I$^-$ concentration, the Bi 4$f_{5/2}$ and 4$f_{7/2}$ peaks systematically red shift, suggesting the interlayer iodine anions enrich the electronic density of Bi-O bonds. This inference is verified by the O *1s* XPS spectra (Fig. 4b) where the red shifts of the O1s for the BiOBr$_x$I$_{1-x}$ solid solutions are notable as compared to those of the pure BiOBr. Red-shifts of characteristic core level binding energies of Br$^-$ are also remarkable for BiOBr$_x$I$_{1-x}$

11

solid solutions, as shown in the Br 3d XPS spectra in Fig. 4c. The red shifts observed in binding

energy for Bi, O, and Br in the BiOBr$_x$I$_{1-x}$ samples, corresponding to increased core electron

density, were thought to arise from the electron-donating effects from iodine anions. The

inference is reasonable as considering the lower electronegativity (2.66) of iodine than Br (2.96),

which is verified by the gradual blue-shifts of the 3d XPS peaks of iodine (Fig. 4d) when

decreasing the iodine concentration (ie. Increasing x). Meanwhile, the intensity of the 3d XPS

peaks of iodine (Fig. 4d) increases while the Br 3d XPS decreases (Fig. 4c) as decreasing the

amount of I$^-$ in the BiOBr$_x$I$_{1-x}$ compound. Moreover, for the BiOBr and BiOI samples, the state of

the art DFT simulations revealed the conduction bands (CB) are mainly composed of Bi 6p and

the valence bands (VB) of Br 4p and iodine 5p orbitals[7, 14], respectively. Therefore, electronic

donation effects from iodine in the BiOBr$_x$I$_{1-x}$ samples are expected to revise the band edges of

the samples, which are discussed further below.

3.5 Band structures

3.5.1 The Valence Band Maximum (VBM) Measured by XPS

Because the band edges are crucial to determining their redox ability, it is necessary to explore

the dependence of band edges (CBM and VBM) on x and the compound electronegativity [7].

The VBM energies of the BiOBr$_x$I$_{1-x}$ samples can be determined by valence band XPS, as

presented in Fig.5. Their fermi levels were corrected by work function of gold and the relative

VBM energy positions are determined by tangent of XPS edges to inceptions on the binding

energy axis. VBM energies of the BiOBr$_x$I$_{1-x}$ samples vary from 1.3 eV (of BiOI) to 2.3 eV (of

BiOBr) as increases x from 0 to 1. Since the work function of gold (5.3 eV) is 0.8 eV more

positive than standard electrode potential of reverse hydrogen electrode (RHE, 4.5 eV versus

vacuum), the VBM positions obtained from VB XPS correspond to 2.1 to 3.1 eV in RHE scale,

which is very close to those calculated using Mulliken electronegativity method (see section

3.5.2). Moreover, the measured VBM of BiOBr is deeper than that of BiOI, reflecting the VBM

12

position is highly dependent on the electronegativity of constituent halogen anions, agreeing

with previous DFT simulations.[27]
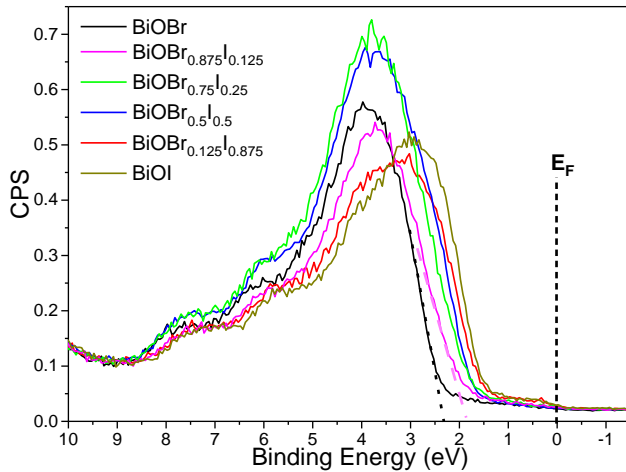
Figure 5. The corrected valence band XPS spectra of the $BiOBr_xI_{1-x}$ samples

On the other hand, as shown in Fig. 5, increasing iodine concentration (reducing x) in $BiOBr_xI_{1-x}$

solid solutions results in red shift of VBM. The red shift of VBM is significant even with a small

portion of iodine substitution of Br can greatly lift the VBM position to more electronegative.

Because of the small difference of VBM energies between the VBM XPS measurements and

the calculated from Mulliken electronegativity method, the CBM energies were calculated to

correlate band edges and the halogen elements,[7, 28] as discussed in 3.5.2.

3.5.2   The dependence of band edges on Br/I concentration

For a semiconductor, its electronic levels in the valence band are occupied and the levels in the

conduction band are empty. The Mulliken electronegativity method has been widely applied to

estimate the band edges of semiconductor with adequate theoretical foundation for rapidly

grabbing the characteristics of band structure for a given Eg and sample composition. This

method presumes the energy of the valence band edge of the bulk material, E_{VBM}, is a measure

of the ionisation potential (I) referring to vacuum potential energy of zero. The conduction band

13

edge energy, E_{CBM}, is a measure of the electron affinity, A, of the compound. The Fermi level is the absolute electronegativity, $-\chi$, of a semiconductor.[21] The relationship between the Eg and electronegativity can be expressed by equation 2~3:

$$E_{CBM} = -A = |\chi| - 0.5\ E_g = \chi - E^e - 0.5\ E_g \qquad \ldots\ldots\ldots\ldots(2)$$

$$E_{VBM} = -I = |\chi| + 0.5\ E_g = \chi - E^e + 0.5\ E_g \qquad \ldots\ldots\ldots\ldots(3)$$

Where χ of a compound can be expressed *via* the geometric mean of the absolute electronegativity of the constituent atoms, and the electronegativity of individual atom is defined as the arithmetic mean of the atomic electron affinity (A) and the first ionisation energy (I). For instance, the electronegativity of Bi (χ_{Bi}) and $BiOBr_{0.75}I_{0.25}$ sample ($\chi_{BiOBr0.75I0.25}$) can be calculated via eq. 4-5:

$$\chi_{Bi} = (I_{Bi} + A_{Bi})/2 \qquad \ldots\ldots\ldots..(4)$$

$$\chi_{BiOBr0.75I0.25} = (\chi_{Bi}{}^* \chi_O{}^* \chi_{Br}{}^{0.75*} \chi_I{}^{0.25})^{1/3} \ldots\ldots\ldots..(5)$$

where E^e is the energy of free electrons on the hydrogen scale (~4.5 eV), and E_g is the band gap energy of the semiconductor.[16]

The calculated energy levels of VBM and CBM are listed in Table 1, from which one can clearly see the dependence of band edges on Br ratio, x. As decreasing x or increasing amount of iodine concentration, the E_{CBM} becomes more positive (less reductive) whist the E_{VBM} potentials more negative (shift up, less oxidative). Moreover, it is notable the low iodine concentration causes more significant shifts of VBM and CBM simultaneously, agreeing to VB XPS results. Apparently, the structural iodine is not only lift up VBM but also bring down the CBM.

3.6 Photocatalytic Activities
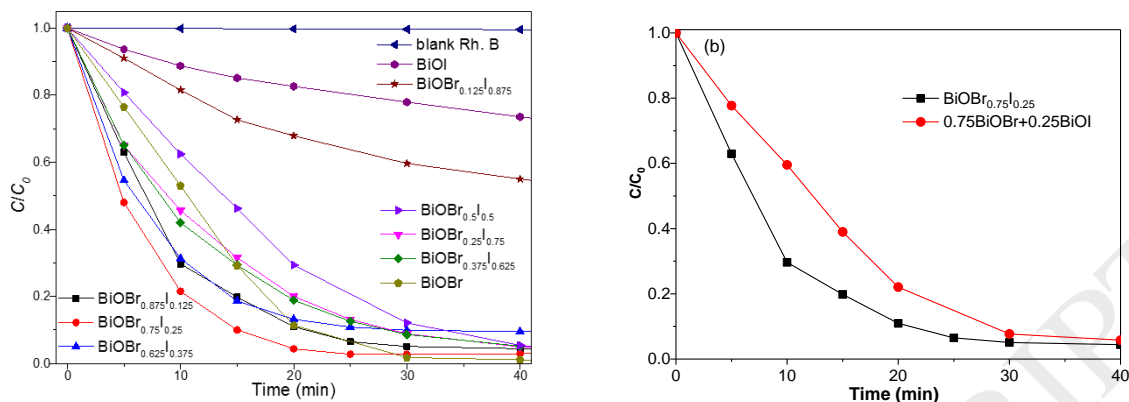
Figure 6. Visible-light ($\lambda \geq 400$ nm) photodegradation of RhB (20 ppm aqueous solution) on the

BiOBr$_x$I$_{1-x}$ samples (a), and comparison between solid solution and mechanical mixtures (b).

Fig. 6a shows the temporal RhB concentration changes on the BiOBr$_x$I$_{1-x}$ catalysts under visible

light illumination, revealing their photocatalytic activity depends on their halogen concentrations.

A slight increase of iodine concentration in the BiOBr$_x$I$_{1-x}$ solid solutions at high Br concentration

(x>0.75) can promote photocatalytic activity, though the activity is impaired as further increasing

iodine concentration (i.e. reducing x). From the activity curves, the reaction kinetic rate

constants (*k*) of the BiOBr$_x$I$_{1-x}$ solid solutions were calculated through $-kt = ln\ (C/C_0)$ and listed in

Table 1.

Both the temporal photocatalytic activity and the kinetic constants indicate that the apparent

photocatalytic activity of the BiOBr$_x$I$_{1-x}$ catalysts decreases follow the sequence: BiOBr$_{0.75}$I$_{0.25}$ >

BiOBr$_{0.875}$I$_{0.125}$ ≈ BiOBr$_{0.625}$I$_{0.375}$ > BiOBr > BiOBr$_{0.375}$I$_{0.625}$ > BiOBr$_{0.25}$I$_{0.75}$ > BiOBr$_{0.5}$I$_{0.5}$ >

BiOBr$_{0.125}$I$_{0.875}$ > BiOI. The BiOBr$_{0.75}$I$_{0.25}$ sample of relatively small Eg and positive VBM

displayed the highest photocatalytic activity under visible light irradiation. In addition, compared

to BiOI (Eg ~1.8 eV [21]), BiOBr (Eg ~2.8 eV [29]) possesses larger Eg but higher photocatalytic

activity because of its more positive VBM. The above photocatalytic activity results suggest that

15

both the Eg and bandstructure, in particular the VBM positions, determines the RhB

photodegradation activity of the $BiOBr_xI_{1-x}$ solid solution photocatalysts.

Furthermore, as shown in Fig.6b, the RhB photodegradation activity of $BiOBr_{0.75}I_{0.25}$ is observed

of higher activity than the physically mixed catalysts containing BiOBr and BiOI in molar ratio of

0.75:0.25, verifying the effectiveness of forming a solid solution for promoting photocatalytic

activity. We suppose that the solid solution catalysts takes the advantages of the fine-tuned

electronic band structure (Eg and band edges), whereas the low activity of the mixed

photocatalyst of BiOBr and BiOI acted independently without synergism. The latter is not a Z-

scheme catalyst because no charge shuttle agent was applied in our experiments.[27]

4. Discussion

4.1 Dependence of bandstructure on compound electronegativity

The above results revealed that introducing more electronegative iodine (χ_I=2.66) into BiOBr

successfully decreases the compound electronegativity of resultant solid solution $BiOBr_xI_{1-x}$ and

changes their band structures (Eg, VBM and CBM). It is reasonable that substitution of X anions

in BiOX can modulate the VBM because the VBMs of BiOBr and BiOI are composed of O $2p$

and X np hybrid orbitals [7, 14]. X np orbitals are the main components of BiOX VBM, thus the X

element of low-electronegativity occupy the VBM top and play core roles to modulate VBM

electron behaviour. As for the contributions of X elements to CBM of the $BiOBr_xI_{1-x}$ solid

solutions, previous DFT simulation results of BiOBr and BiOI suggest that their CBMs are

mainly composed of Bi 6p orbitals and the direct contribution from X elements is negligible [7,

17]. Therefore, the addition of iodine into BiOBr matrix modulates the CBM via perturbing the

electronic configuration of $[Bi_2O_2]^{2+}$ slab, in particular that of bismuth cations. This inference is

confirmed by red shits of core level XPS spectra of Bi and O (see section 3.5).

16

Calculated using the Mulliken electronegativity method, the energy band diagrams presented in Fig.7A clearly indicate that the formation of $BiOBr_xI_{1-x}$ solid solutions can well tune the bandstructure, both the Eg and energy band edges (CBM and VBM), via adjusting Br/I concentration. However, the method cannot clarify the exact band composition of CBM and VBM and the orbital contributions from the compositional halogen elements. The in-depth investigation for the detailed influences of iodine on the bandstructures of the $BiOBr_xI_{1-x}$ solid solutions are undertaking, using recently established methodology combining DFT and photoelectrochemical characterisations[7].

4. 2 Correlation photocatalysis with bandstructure

There have always been contradictions between the enhanced visible-light absorption and the redox capability.[13] Jia and co-workers demonstrated that 3D-structured $BiOBr_xI_{1-x}$ (0<x<1) samples possessed higher photocatalytic activities than pristine BiOBr (x=1) and BiOI (x=0), with the highest photocatalytic activity observed on $BiOBr_{0.6}I_{0.4}$ [22]. Their 3D BiOBr displayed the weakest photocatalytic activity although it possessed highest surface area and the 3D BiOI displayed the second worst activity despite its strongest visible light absorption. The authors attributed those activity behaviour to synergism between surface area, porosity and band structures (smaller Eg and VBM positions), but it is ambiguous in identifying the predominant factor in photocatalytic reaction.

In our research, the samples are of very similar morphologies and comparable surface areas, enabling us to clarify the influences of bandstructure on their photocatalytic activity. The photocatalysis is a complex process involving bandgap-limited excitation, effective charge carrier transfer (separation, transport and recombination) and surface redox reactions [1], while it was argued the light absorption and surface area of the photocatalyst are dominant factors for the photocatalytic reaction[30]. This argument inspired us to plot Eg and kinetic constants of

17

BiOBr$_x$I$_{1-x}$ (0≤x≤1) samples versus the x value. As presented in Fig 2b, it seems there is no direct linear correlation between Eg and photocatalytic reaction rates on the BiOBr$_x$I$_{1-x}$ (0≤x≤1) samples.
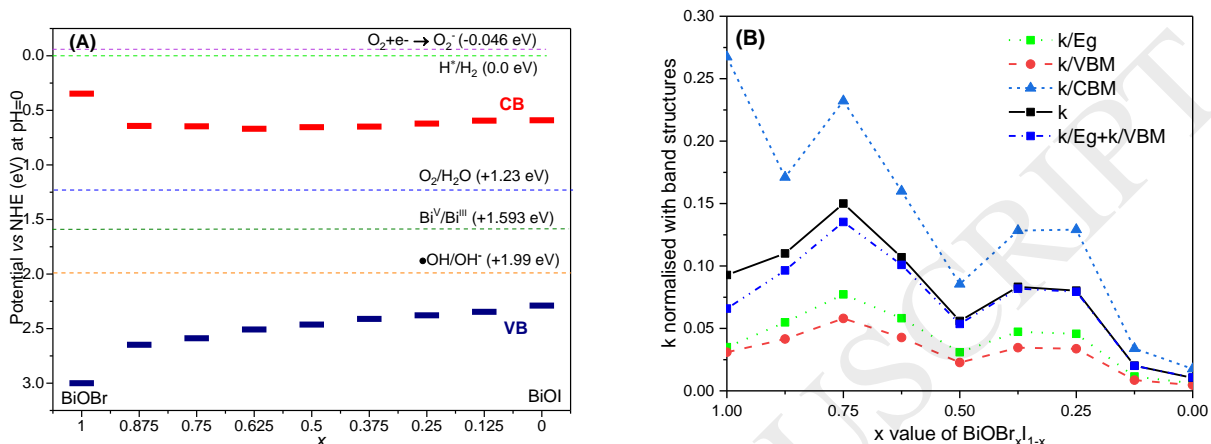

Figure 7 Band positions (A) and the normalisation of kinetic constants with bandstructure energies of the BiOBr$_x$I$_{1-x}$ solid solutions

As widely applied in the DFT simulation, single electron model was assumed for simplifying the analysis of complex sequential processes. Taking the similar assumption, the photocatalytic decolourisation of RhB can be looked as a complex process embracing elementary processes of light excitation, effective charge carriers (depending on separation, transfer, transport and recombination) and surface redox reactions. The individual processes will have their own kinetic activation energy: excitation is determined by Eg, effective charge due to CBM or VBM, and surface reaction due to the surface adsorption amount determined surface geometry for specific adsorbent. The SEM results suggested the samples are in similar morphology, so the surface geometric factor could be negligible. Applying the above assumption, as shown in Fig.7b, we can further normalise the kinetic constants with the Eg and band edges of the BiOBr$_x$I$_{1-x}$ (0≤x≤1) samples to investigate the sensitivity of *k* (apparent kinetic constants) over the bandgap and band edges.

18

From Fig.7b one can see that the kinetic constant curve is almost overlapping with the curve of the summed k/Eg and k/E$_{VBM}$, suggesting the k values are probably related to the synergism of VBM and light absorption which is determined by bandgap (both Eg value and transition mode of excitons). It is notable that the k ~ x curve fully overlaps with the sum curve of (k/Eg+k/VBM) when x≤0.5, implying that the light absorption and VBM dominate photocatalytic activity. This is reasonable because their light absorption (beyond 650 nm) can cover the whole spectrum of RhB and thus screen the dye-sensitisation effects. As x>0.5, the sum curve is lower than the k curve, suggesting there is another factor affecting their reaction rates. We suppose it would be the dye-sensitisation effects, which is reasonable as the light absorption of these photocatalysts cannot fully cove the RhB spectrum. This inference is supported by that the greater x leads to larger difference of the (k/Eg+k/VBM) sum curve from the k curve, where photocatalysts light absorption differs from RhB spectrum greatly.

Moreover, the k/CBM is much higher than k curve that could rule out the CBM dominating RhB photodegradation. The curves of k/Eg and k/E$_{VBM}$ take the similar trend of the k curve and the k/E$_{VBM}$ showed the lowest value, which probably indicates the photocatalytic reaction rate is more determined by the VBM position. The large difference between k/E$_{CBM}$ for the x>0.625 suggests both the CBM or dye sensitisation contributes to the photocatalytic reaction on those catalysts. The discussion of Fig.7b well agree with the experimental analyses of rate-limiting steps as previously reported for BiOX photocatalysts [7, 9, 16, 26].

In the sensitivity analysis, we ignored the contributions of recombination of charge carriers and surface reaction, which is reasonable because the previous experimental study suggested the recombination is not a key factor and the surface chemical reaction is ultrafast [7]. Moreover, the k/Eg may reasonably reflect the dependence on light absorption that is also influenced by

the RhB spectrum, while the k/VBM may reflect how the oxidation power of VBM holes affect k. Although the above discussions regarding the dependence of k on the Eg and VBM are interesting and consistent with the photocatalytic phenomena on our $BiOBr_xI_{1-x}$ samples, the science behind the mathematical treatment is not rigid because we cannot rule out the treatment is just a coincidence herein. Although the reaction kinetics was resonated according to Arrhenius theory (supporting information), such kinetic sensitivity analysis method needs to be further explored and verified by sampling from more different solid solution photocatalyst systems. We presented the sensitivity analysis here in order to inspire further theoretical research in the scientific community.

4.3 The rate-limiting active species

It is important to correlate the photocatalysis with photogenerated active species at energy levels of band edges in the photocatalytic reaction system. The calculated VBM potentials of all the $BiOBr_xI_{1-x}$ samples are located far below the standard redox potential of $\cdot OH/OH^-$ (1.99 eV), suggesting that the photogenerated hole at VBM is more oxidative than hydroxyl radical. However, the photogenerated h^+ could not oxidise OH^- to generate the $\cdot OH$ radicals because of the stronger adsorption and the more negative reduction potentials of RhB.

The CBM potential of the $BiOBr_xI_{1-x}$ samples is not strong enough to reduce the O_2 into the superoxygen radical ($\cdot O_2^-$) *via* the photoexcited electrons, because the electrochemical potential for single electron reduction of oxygen is -0.046 eV.[31] The electrons may be leading to the reduction of Bi cations within the structure or reduction of dissolved oxygen because of the more preferential potentials of O_2/H_2O, Bi^{III}/Bi^0 (0.5 eV vs NHE) and Bi^V/Bi^{III} [32].

The above discussions suggest that it is theoretically reasonable that the photodegradation of RhB is mainly due to the photogenerated h^+ rather than photogenerated $\cdot OH$ or $\cdot O_2^-$ radicals on

the $BiOBr_xI_{1-x}$ samples. Therefore, the present research suggests the formation of hetero-halogen BiOX is an effective strategy to tune band structures and photocatalytic activity.

5   Conclusion

A series of $BiOBr_xI_{1-x}$ solid solutions with a controlled band structure were successfully synthesised by an effective and rapid one-step ultrasonication method. The samples were well characterised with XRD, UV-Vis-DRS, SEM and XPS techniques. The incorporation of iodine into BiOBr to form $BiOBr_xI_{1-x}$ solid solutions can cause significant crystal distortion and strong deviation of lattice parameters from Vegard's law, with more significant deviation of lattice parameter c. The band gaps of the $BiOBr_xI_{1-x}$ solid solutions nonlinearly decrease as increasing the iodine concentration, because the incorporation of more electronegative iodine can not only lift the VBM but also bring down CBM positions as demonstrated in the band energy diagram. The iodine substitutions of Br within x=0.875~0.75 dramatically reduce bandgap though further increasing iodine concentration influences bandstructure less significantly.

The RhB photodegradation activity declines in the order of $BiOBr_{0.75}I_{0.25}$ > $BiOBr_{0.875}I_{0.125}$ ≈ $BiOBr_{0.625}I_{0.375}$ > BiOBr > $BiOBr_{0.375}I_{0.625}$ > $BiOBr_{0.25}I_{0.75}$ > $BiOBr_{0.5}I_{0.5}$ > $BiOBr_{0.125}I_{0.875}$ > BiOI. The sensitivity analysis suggests visible-light photocatalytic activity on the $BiOBr_xI_{1-x}$ solid solutions not only depending on the bandgap but also the VBM potentials. The Mulliken electronegativity analysis allows to conclude that the photogenerated holes on VBM are the rate-limiting species of the photocatalytic reaction. The optimised $BiOBr_{0.75}I_{0.25}$ photocatalyst is superior to the mechanically mixed catalysts with BiOBr/BiOI molar ration at 0.75/0.25 and same catalyst loading, verifying the effectiveness to design solid solution photocatalysts.

Acknowledgement

21

References

[1] X. Chen, Z. Zhang, L. Chi, A.K. Nair, W. Shangguan, Z. Jiang, Recent Advances in Visible-Light-Driven Photoelectrochemical Water Splitting: Catalyst Nanostructures and Reaction Systems, Nano-Micro Lett., 8 (2016) 1-12.

[2] S. Rawalekar, T. Mokari, Rational Design of Hybrid Nanostructures for Advanced Photocatalysis, Adv. Energy Mater., 3 (2013) 12-27.

[3] C.S. Uyguner-Demirel, N.C. Birben, M. Bekbolet, Elucidation of background organic matter matrix effect on photocatalytic treatment of contaminants using TiO_2: A review, Catal Today, 284 (2017) 202-214.

[4] S. Kundu, A. Patra, Nanoscale Strategies for Light Harvesting, Chem. Rev., 117 (2017) 712-757.

[5] X. Meng, Z. Zhang, Bismuth-based photocatalytic semiconductors: Introduction, challenges and possible approaches, J. Mol. Catal. A: Chem., 423 (2016) 533-549.

[6] R. Qian, H. Zong, J. Schneider, G. Zhou, T. Zhao, Y. Li, J. Yang, D.W. Bahnemann, J.H. Pan, Charge carrier trapping, recombination and transfer during TiO2 photocatalysis: An overview, Catalysis Today, (2018).

[7] J. Guo, X. Liao, M.-H. Lee, G. Hyett, C.-C. Huang, D.W. Hewak, S. Mailis, W. Zhou, Z. Jiang, Experimental and DFT insights of the Zn-doping effects on the visible-light photocatalytic water splitting and dye decomposition over Zn-doped BiOBr photocatalysts, Applied Catalysis B: Environmental, 243 (2019) 502-512.

[8] K. Zhang, W. Zhou, L. Chi, X. Zhang, W. Hu, B. Jiang, K. Pan, G. Tian, Z. Jiang, Black N/H-TiO_2 Nanoplates with a Flower-Like Hierarchical Architecture for Photocatalytic Hydrogen Evolution, ChemSusChem, 9 (2016) 2841-2848.

[9] L. Kong, Z. Jiang, T. Xiao, L. Lu, M.O. Jones, P.P. Edwards, Exceptional visible-light-driven photocatalytic activity over BiOBr-$ZnFe_2O_4$ heterojunctions, Chem. Commun., 47 (2011) 5512-5514.

[10] S. Na Phattalung, S. Limpijumnong, J. Yu, Passivated co-doping approach to bandgap narrowing of titanium dioxide with enhanced photocatalytic activity, Appl. Catal. B: Environ., 200 (2017) 1-9.

[11] F. Zou, Z. Jiang, X. Qin, Y. Zhao, L. Jiang, J. Zhi, T. Xiao, P.P. Edwards, Template-free synthesis of mesoporous N-doped SrTiO3 perovskite with high visible-light-driven photocatalytic activity, Chemical Communications, 48 (2012) 8514-8516.

[12] J.H. Pan, C. Shen, I. Ivanova, N. Zhou, X. Wang, W.C. Tan, Q.-H. Xu, D.W. Bahnemann, Q. Wang, Self-Template Synthesis of Porous Perovskite Titanate Solid and Hollow Submicrospheres for Photocatalytic Oxygen Evolution and Mesoscopic Solar Cells, ACS Applied Materials & Interfaces, 7 (2015) 14859-14869.

[13] S. Ouyang, J. Ye, β-$AgAl_{1-x}Ga_xO_2$ Solid-Solution Photocatalysts: Continuous Modulation of Electronic Structure toward High-Performance Visible-Light Photoactivity, J. Am. Chem. Soc., 133 (2011) 7757-7763.

[14] X.-P. Lin, F.-Q. Huang, W.-D. Wang, Z.-C. Shan, J.-L. Shi, A series of Bi-based oxychlorides as efficient photocatalysts, Key Engineering Materials, 368-372 (2008) 1503-1506.

[15] J. Lu, Q. Meng, H. Lv, L. Shui, M. Jin, Z. Zhang, Z. Chen, M. Yuan, X. Wang, J.-M. Liu, G. Zhou, Synthesis of visible-light-driven $BiOBr_xI_{1-x}$ solid solution nanoplates by ultrasound-assisted hydrolysis method with tunable bandgap and superior photocatalytic activity, J Alloys Compd, 732 (2018) 167.

[16] Z. Jiang, F. Yang, G. Yang, L. Kong, M.O. Jones, T. Xiao, P.P. Edwards, The hydrothermal synthesis of BiOBr flakes for visible-light-responsive photocatalytic degradation of methyl orange, J. Photochem. Photobiol. A: Chem., 212 (2010) 8-13.

[17] Y. Liu, W.-J. Son, J. Lu, B. Huang, Y. Dai, M.-H. Whangbo, Composition Dependence of the Photocatalytic Activities of $BiOCl_{1-x}Br_x$ Solid Solutions under Visible Light, Chem. Eur. J., 17 (2011) 9342-9349.

[18] A. Coelho, TOPAS and TOPAS-Academic: an optimization program integrating computer algebra and crystallographic objects written in C++, Journal of Applied Crystallography, 51 (2018) 210-218.

[19] X. Zong, H. Yan, G. Wu, G. Ma, F. Wen, L. Wang, C. Li, Enhancement of Photocatalytic H_2 Evolution on CdS by Loading MoS_2 as Cocatalyst under Visible Light Irradiation, J. Am. Chem. Soc., 130 (2008) 7176-7177.

[20] Y. Wang, K. Deng, L. Zhang, Visible Light Photocatalysis of BiOI and Its Photocatalytic Activity Enhancement by in Situ Ionic Liquid Modification, J. Phys. Chem. C, 115 (2011) 14300-14308.

[21] J. Cao, B. Xu, H. Lin, B. Luo, S. Chen, Chemical etching preparation of BiOI/BiOBr heterostructures with enhanced photocatalytic properties for organic dye removal, Chem. Eng. J., 185–186 (2012) 91-99.

[22] Z. Jia, F. Wang, F. Xin, B. Zhang, Simple Solvothermal Routes to Synthesize 3D $BiOBr_xI_{1-x}$ Microspheres and Their Visible-Light-Induced Photocatalytic Properties, Ind. Eng. Chem. Res., 50 (2011) 6688-6694.

[23] A.F. Wells, Structural Inorganic Chemistry, Structural Inorganic Chemistry1971, pp. 1095.

[24] E. Keller, V. Krämer, A Strong Deviation from Vegard's Rule: X-Ray Powder Investigations of the Three Quasi-Binary Phase Systems BiOX-BiOY (X, Y = Cl, Br, I) Zeitschrift für Naturforschung B, 60 (2005) 1255-1263.

[25] M.A. Butler, Photoelectrolysis and physical properties of the semiconducting electrode WO_2, J. Appl. Phys., 48 (1977) 1914-1920.

[26] L. Kong, Z. Jiang, H.H. Lai, R.J. Nicholls, T. Xiao, M.O. Jones, P.P. Edwards, Unusual reactivity of visible-light-responsive AgBr–BiOBr heterojunction photocatalysts, Journal of Catalysis, 293 (2012) 116-125.

[27] W.L. Huang, Q. Zhu, Structural and electronic properties of BiOX (X=F, Cl, Br, I) considering Bi 5f states, Comput. Mater. Sci., 46 (2009) 1076-1084.

[28] D.S. Bhachu, S.J.A. Moniz, S. Sathasivam, D.O. Scanlon, A. Walsh, S.M. Bawaked, M. Mokhtar, A.Y. Obaid, I.P. Parkin, J. Tang, C.J. Carmalt, Bismuth oxyhalides: synthesis, structure and photoelectrochemical activity, Chemical Science, 7 (2016) 4832-4841.

[29] S.Y. Chai, Y.J. Kim, M.H. Jung, A.K. Chakraborty, D. Jung, W.I. Lee, Heterojunctioned $BiOCl/Bi_2O_3$, a new visible light photocatalyst, J. Catal., 262 (2009) 144-149.

[30] F.E. Osterloh, Photocatalysis versus Photosynthesis: A Sensitivity Analysis of Devices for Solar Energy Conversion and Chemical Transformations, ACS Energy Letters, 2 (2017) 445-453.

[31] D. Wang, T. Kako, J. Ye, Efficient Photocatalytic Decomposition of Acetaldehyde over a Solid-Solution Perovskite $(Ag_{0.75}Sr_{0.25})(Nb_{0.75}Ti_{0.25})O_3$ under Visible-Light Irradiation, J. Am. Chem. Soc., 130 (2008) 2724-2725.

[32] H. Fu, C. Pan, W. Yao, Y. Zhu, Visible-Light-Induced Degradation of Rhodamine B by Nanosized Bi_2WO_6, J. Phys. Chem. B, 109 (2005) 22432-22439.